

# A topologically stabilized metastable fluid in a system of cylindrically confined hard spheres.

Mahdi Zarif<sup>\*,†</sup> and Richard K. Bowles<sup>\*,‡,¶</sup>

<sup>†</sup>*Department of Physical and Computational Chemistry, Shahid Beheshti University, Tehran 19839-9411, Iran.*

<sup>‡</sup>*Department of Chemistry, University of Saskatchewan, SK, S7N 5C9, Canada.*

<sup>¶</sup>*Centre for Quantum Topology and its Applications (quanTA), University of Saskatchewan, SK S7N 5E6, Canada.*

E-mail: m\_zarif@sbu.ac.ir; richard.bowles@usask.ca

## Abstract

Metastability in soft condensed matter systems usually results from the presence of a nucleation free energy barrier and/or slow dynamics caused by high density jamming phenomena. Here, we use molecular dynamics and Monte Carlo simulation to show that the interactions between topological defects stabilizes a chiral helical fluid in a confined quasi-one-dimensional hard sphere fluid dramatically slowing its decay toward the equilibrium achiral fluid state. Analysis of thermodynamic, structural and dynamic properties of the system show the equation of state bifurcates continuously at intermediate pressures into two distinct branches that are accessed from different initial conditions, but terminate at the same close packed single helix in the high pressure limit. The equilibrium fluid, which forms the high pressure branch as the system is compressed from low density, is characterized by helical sections separated by randomly distributed topological defects that change the helical twist direction giving rise to an achiral fluid. The low pressure metastable branch, formed by decompressing the system

from the perfect helix, is characterized by the appearance of loosely paired defects that help retain the chiral excess of the original state and stabilize the fluids until it merges continuously with the equilibrium branch at intermediate pressures.

## Keywords

Confined Fluid, Hard Spheres, Topological, Defects, Molecular Dynamics, Monte Carlo

## Introduction

Topological order and topologically protected states usually appear in correlated quantum systems<sup>1</sup> but there is growing evidence to suggest that they can also play an important role in the properties of classical systems.<sup>2-4</sup> For example, Zygmunt et al.<sup>5</sup> found that dense packings of anisotropic colloids form topological phases that retain near perfect order below close packing, demonstrating a form of classical topological protection. The origin of topological order in these systems differs from those of their quantum counterparts and arises from the organization of particle contacts within the unit cell of the packing which suggests other colloidal systems may exhibit similar phenomena.

The geometric confinement of hard sphere particles to narrow quasi-one-dimensional (quasi-1d) channels leads to the spontaneous formation of helical structures<sup>6-8</sup> ranging from simple single helices through to multi-stranded helices with slip or staggered structures, depending on the channel diameter. When the channel diameter is sufficiently narrow, all the particles in the dense packings contact the channel wall, which allows their structures, and the transitions between them, to be described in terms of phyllotactic disk arrangements on a plane.<sup>9-12</sup> A variety of new structures arise as the channel becomes wide enough for particles to enter the core of the packings<sup>13,14</sup> and eventually, the appearance of bulk face-centred-cubic (FCC) crystal packing arrangements leads to the formation of complex core-shell structures.<sup>15</sup> A similar array of structures have been found in confined quasi-1d

soft sphere systems,<sup>16,17</sup> and have been observed experimentally in molecular nanotube systems,<sup>18–20</sup> colloidal particles<sup>14,21–23</sup> and macroscopic, athermal systems.<sup>24</sup> Introducing particle shape anisotropy then broadens the range of structural motifs formed under cylindrical confinement and can generate new chirality elements.<sup>25,26</sup>

Colloidal crystals have applications in photonics<sup>27–30</sup> and these helical packings of hard spheres exhibit chiral photonic properties.<sup>31</sup> However, quasi-one-dimensional systems with short ranged interactions generally do not exhibit phase transitions<sup>32,33</sup> because there is always an entropic advantage to introducing a defect into the system that overcomes the energetic cost of the defect in the thermodynamic limit.<sup>34</sup> Randomly distributed defects would break up the helical structure, leading to an achiral fluid. Nevertheless, there are circumstances where phase transitions can occur in quasi-one dimensional systems<sup>35,36</sup> and phase transitions can arise in 1d systems when the particle interactions become long-range and the defects have a topological character.<sup>37–39</sup>

The current work examines the role helical topology plays in the structural, thermodynamic and dynamic properties of a system of hard spheres confined to a narrow, quasi-1d channel, focusing on a system that has the simplest, perfect single helix ground state.<sup>40,41</sup> To capture the topological properties of the fluid, we use an analysis (see Methods) that identifies structural “defects” in fluid where the twist direction of the helix changes, i.e. between left ( $\mathcal{M}$ ) and right ( $\mathcal{P}$ ) twist directions. The method provides an approximate mapping of a fluid configuration to its local jammed, or inherent structure,<sup>42–44</sup> which helps us relate the thermodynamics and dynamics of the fluid to its underlying topological structure through the number and distribution of the helical defects.

Previously,<sup>40,45</sup> it has been shown that defects in the jammed helical packing appear in pairs and the structure of the helix between two defects is fundamentally changed to that of an asymmetric double helix with a pitch that depends on their distance of separation. This affects the packing density of the system as a function of position of the defects and leads to an effective, entropically driven, long range attraction between isolated defect pairs.

Such a topological, long range interaction could, in principle, lead to phase transition. Fu et al<sup>14</sup> found, using  $N, P, T$  Monte Carlo (MC) simulations, that initial low and high density starting conditions converged to a single equation of state (EOS) at low pressure, but the two different starting conditions did not converge at high pressure. Hu et al<sup>46</sup> used the transfer matrix method to show that correlation lengths in the system remain finite, ruling out the possibility of a phase transition at the bifurcation point of the two branches of the EOS.

However, the topological properties of the two branches of the EOS have not been examined. Here, we show that, contrary to expectations, the high pressure branch of the EOS of this system represents the equilibrium fluid where the defects in the helical structure are randomly distributed, ensuring the fluid is achiral. The second, low pressure branch formed by decompressing the system from a perfect helix at high density, maintains an excess helical twist in one direction, exhibits slow relaxation times and remains stable for long simulation times at densities where the higher pressure equilibrium fluid rapidly relaxes. This suggests the topology of the helical twist plays a role in the system's properties, and provides a degree of stabilization for the chiral state. The details of the model and simulations methods can be found in the Methods section.

## Results

Figure 1(a) shows the pressure EOS for the system over a wide range of densities. Below  $P_L/kT \approx 38$  both compression and decompression simulations follow the same EOS, which exhibits a small shoulder centred at  $P_L/kT \approx 15$  ( $\phi \approx 0.25$ ) and approaches ideal gas behaviour in the low density limit. At higher densities, we see two distinct branches of the EOS, a higher pressure branch for compression and a lower pressure branch for decompression. Fig. 1(b) highlights that both branches of the EOS can be reproduced, from their respective initial conditions, using different simulation methods that follow distinct equilibration pathways. The MD simulations move through a sequential series of equilibrium

states, essentially following the EOS as the system is equilibrated at one  $\phi$  before being compressed, or decompressed, to the next. The MC simulation for each state point evolves independently from its starting condition at its assigned constant pressure. Notably, the EOS of the decompression branch is slow to converge, and there is some evidence that the fluid structure still evolves at a very slow rate (see Supporting Information for more details). While we have never observed the system move from one branch of the EOS to the other at  $\phi > 0.33$ , where the bifurcation occurs, if the system is decompressed below this point from either branch, and then recompressed, it always follows the higher pressure branch.

Figure 2(a) shows the heat capacity exhibits distinct peaks for the compression and decompression branches of the EOS, as well as a peak at low pressure, that coincide with changes in the defect fraction,  $\theta = n_d/N$  (see Fig. 2(b)), where  $n_d$  is number of defects, suggesting the fluid goes through a number of structural changes as a function of pressure. We now examine the relationship between the thermodynamic, dynamics and structure in the three distinct regions of the EOS.

### **Low density branch: $\phi < 0.33$ , $P/kT < 38$**

In the ideal gas limit, the system is expected to sample basins in the inherent structure landscape near the maximum of the distribution<sup>44</sup> where  $\theta = (5 - \sqrt{5})/10 \approx 0.276$ .<sup>40</sup> The inset for Figure 2(b) shows that when we perform a direct count of all the defects in the system, highlighted as the MC results,  $\theta \approx 0.35$ . However, if we assume that the unstable environment associated with neighbouring defect pairs leads to their annihilation as the system is compressed to its local inherent structure, then the number of defects decreases and  $\theta \approx 0.3$  (MD results), which is only marginally higher than the expected value. With a high fraction of defects, the number of spheres between the defects is small and the particles tend to adopt linear or zig-zag arrangements. As the pressure increases, the number of defects decreases rapidly before reaching a plateau at  $\theta \approx 0.25$  where the average defect separation is four particles, which corresponds to the smallest section capable of forming part of a

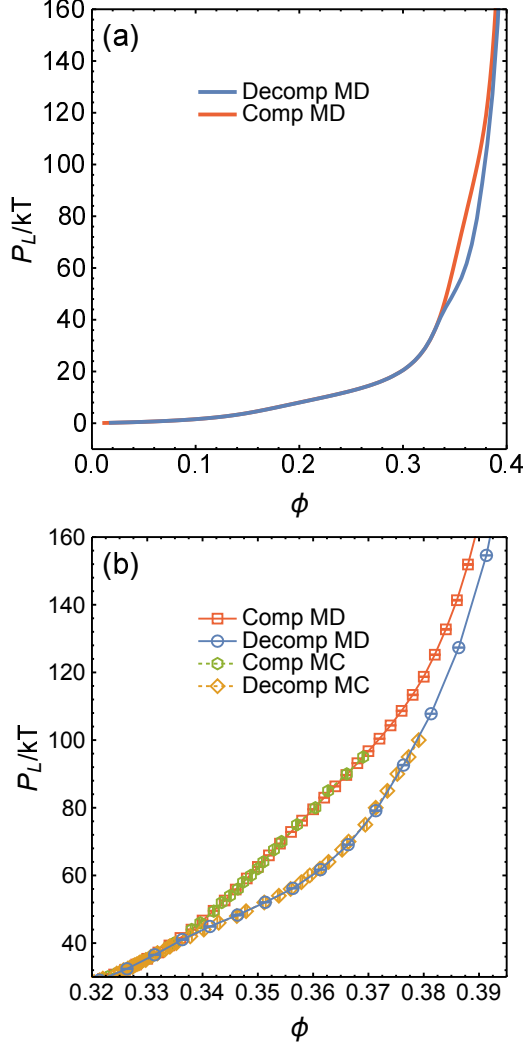


Figure 1: **Equation of state.** (a) MD compression and decompression over full range of  $\phi$  and (b) MD and MC compression and decompression in the high  $\phi$  regime.

helical twist. The number of unstable neighbouring defect environments also becomes small. The helical sections alternate between left ( $\mathcal{M}$ ) and right ( $\mathcal{P}$ ) twist directions and with no preference for one twist direction over the other the excess fraction of ( $\mathcal{P}$ ) tetrahedra,  $f_{\mathcal{P}}$ , remains zero.

**Compression branch:**  $\phi > 0.33$ ,  $P/kT > 38$

The EOS of the compression branch obtained by our MD and MC simulations follows that obtained by Hu et al<sup>46</sup> using the transfer matrix method. The structure of the fluid along the

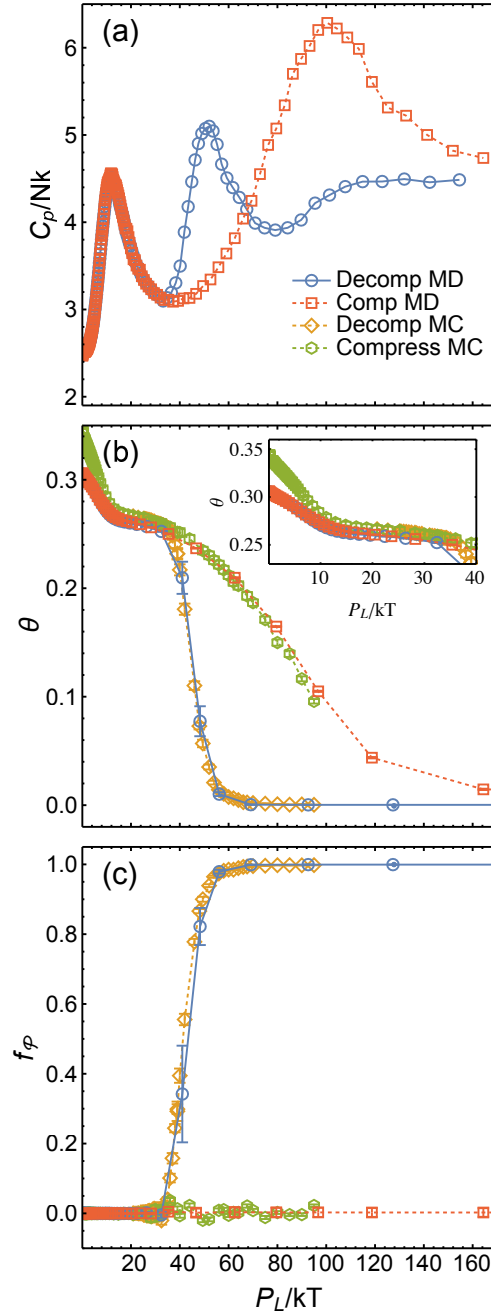


Figure 2: **Comparing thermodynamics, defects and helical excess** (a) Constant pressure heat capacity,  $C_p/Nk$ , (b) defect fraction  $\theta$  (inset: low pressure regime), (c)  $f_{\mathcal{P}}$ , the excess fraction of  $\mathcal{P}$  tetrahedra, as a function of  $P_L/kT$ .

rest of the compression branch consists of loosely organized sections of helix, separated by defects, where all the particles in a given helical section have the same local twist direction and the twist alternates between  $\mathcal{M}$  and  $\mathcal{P}$  directions. With increasing pressure,  $\theta$  begins to decrease again as the fluid continues to move to basins on the inherent structure landscape associated with jammed structures with higher  $\phi_J$ , maximizing its total entropy by trading configurational entropy for increased vibrational entropy. However, eventually the system finds its way toward the bottom of the landscape where there are very few basins, characterized by a small number of defects, and  $\theta$  plateaus again and slowly tends to zero in the limit  $P_L/kT \rightarrow \infty$ , where it will eventually form the perfect helix. The loss of configurational entropy associated with the decrease in  $\theta$  leads to the appearance of the  $C_p$  maximum located at  $P_L/kT \approx 100$  in a process similar to a Schottky anomaly.<sup>47</sup>

The topological nature of the fluid structure means that defects are eliminated in pairs leading to the formation of larger helical sections. Furthermore, as there is no preference for one helical twist direction over another, the defects eliminate randomly and Fig. 2(b) shows  $f_{\mathcal{P}}$  is zero over the entire compression branch of the EOS. Figure 3(a) shows that  $P(n)$ , the probability distribution for helical section sizes, decays exponentially with helical section size at intermediate pressures, before the  $C_p$  maximum. This is consistent with the general form predicted for a random distribution of helical sections, with the exception of the appearance of the single particle section, which is not accounted for in the random model. As the  $C_p$  maximum is approached, the form of the distribution changes, developing a shoulder at  $n \approx 10$  ( $P_L/kT = 90$ ) that evolves into a maximum at higher pressures, above the  $C_p$  maximum. We also see an oscillation in the probabilities for odd and even sized helical sections, with the even helical sections being preferred. The amplitude of the oscillation increases for smaller  $n$  and higher pressure. The same trend was observed in the jammed states of the model and results from the more efficient packing of the even sections.<sup>45</sup>

Figure 4(a) shows that the longitudinal pair correlation function decays exponentially, beyond the small  $n$  region, as expected for a quasi-1D fluid with no long range translational



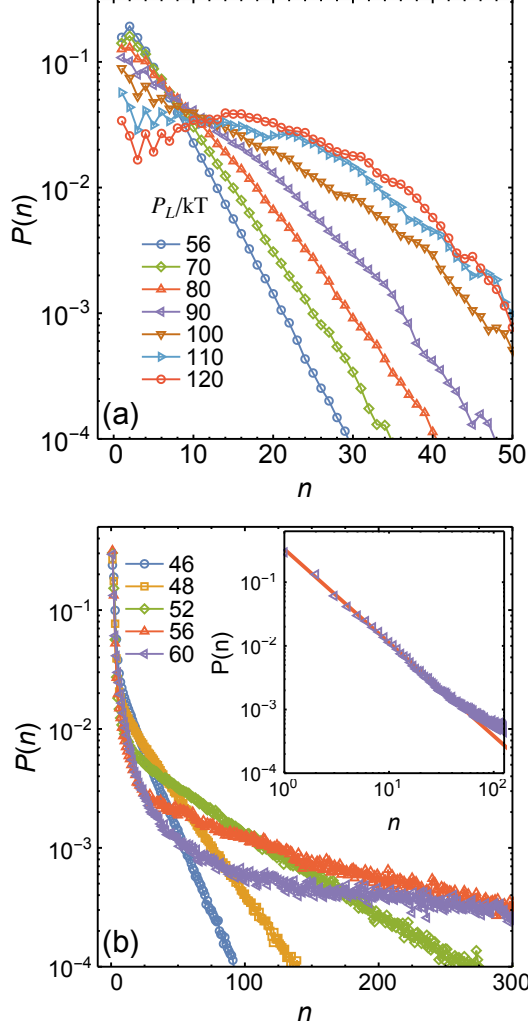


Figure 3: **Helical section length distribution.** Log plots of  $P(n)$  as a function of  $n$  for (a) Compression and (b) Decompression at different pressures. The insert shows a log–log plot of  $P(n)$  for small  $n$  at  $P_L/kT$  on the decompression branch.

order, which also allows us to extract a translational correlation length,  $\xi$ , by fitting the peaks. The insert to Fig. 4(b) shows that  $\xi$  initially grows along the compression branch, but then plateaus above  $P_L/kT \approx 50$ . Similar high pressure plateaus have been observed in the correlation functions of the 2D hard discs next-nearest-neighbour model.<sup>46</sup>

Figure 5(a) shows that along the compression branch of the EOS, the local twist correlation function,  $g_0$ , decays to zero on the time scale of our MD simulations over a wide range of  $\phi$ , including those densities at and above the high pressure heat capacity maximum ( $\phi \approx 0.37, P_L/kT \approx 100$ ), highlighting the fluid-like nature of the system. The time de-

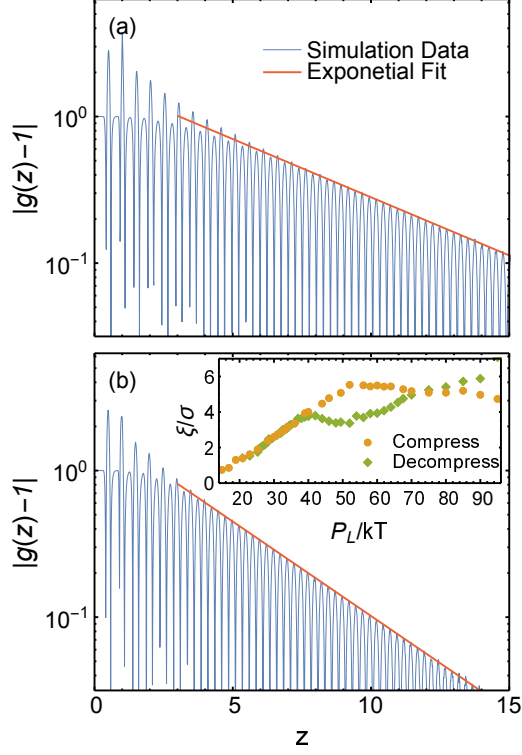


Figure 4: **Longitudinal correlation function and correlation length.** Log plot of  $|g(z) - 1|$  as a function of  $z$  at  $P_L/kT = 52$  for (a) Compression and (b) Decompression simulations. Insert shows the translational correlation function  $\xi/\sigma$  as a function of pressure for compression (circles) and decompression (diamonds).

pendence of  $g_0$  also fits the Kohlraush-Williams-Watts (KWW) function,<sup>48,49</sup>  $\exp[-(t/t_r)^\beta]$ , where  $t$  is time,  $t_r$  is a time constant and  $\beta$  is an exponent that characterizes the nature of the dynamics in a variety of supercooled liquids.<sup>50,51</sup> At low  $\phi$ , we find  $\beta > 1$  (see insert Fig. 5(b)), which indicates the relaxation follows a compressed exponential decay, suggesting the fluid relaxes through a combination of ballistic and diffusive dynamics.<sup>52</sup> When the particles are well separated along the channel, they tend to collide with the channel wall, reversing direction, before particle-particle collisions occur. This generally results in a reversal of the sign of  $v_{tet}$  as the particles cross the channel relative to the other particles that form the tetrahedron of a given particle, and  $g_0$  at low density exhibits negative correlations after a short time (not shown), similar to those observed in the velocity auto-correlation function of bulk hard spheres at low  $\phi$ . With increasing  $\phi$ , particle-particle collisions tend to cage a given particle, maintaining the sign of  $v_{tet}$ , leading to diffusive behaviour and we see  $\beta$  decreases

linearly. Interestingly, we see a change of slope in  $\beta$  at  $\phi \approx 0.33$ , which coincides with density where the helical structure of the liquid begins to develop, and the unstable neighbouring defect environments disappear. At high  $\phi$ ,  $\beta < 1$ , plateauing at  $\beta \approx 0.65$ , which indicates a stretched exponential relaxation that is characteristic of slow glassy dynamics.

Supercooled liquids exhibit a range of behaviour for the temperature dependence of their relaxation times,  $\tau$ .<sup>53</sup> In a strong liquid,  $\tau$  has an Arrhenius temperature dependence,  $\tau \sim \exp(A/T)$  where  $A$  is constant. Fragile liquids exhibit super Arrhenius behaviour that can be described by a number of models, such as the Vogel-Fulcher-Tammann (VFT) equation,<sup>54-56</sup>  $\tau \sim \exp[A/(T - T_0)]$  which predicts a divergence at a finite temperature  $T_0$ , and the parabolic law,<sup>57,58</sup>  $\tau \sim \exp[A/T^2]$ , which predicts no divergence and arises from a facilitated dynamics description of glassy fluids. A 2D system of hard discs confined to a narrow channel<sup>59</sup> even exhibits a crossover from fragile to strong fluid behaviour, located at the  $C_p$  maximum, where the fragile behaviour at low  $\phi$  occurs because defect-defect annihilation create irreversible particle rearrangements that form more stable states. As  $\phi$  increases, the defects become rare and structural relaxation proceeds through the simple hopping events of isolated defects, leading to strong fluid behaviour.

To examine the nature of the dynamics in the current system,  $\tau$  is defined as the time required for  $g_0$  to decay to 0.2. For hard spheres,  $\phi PV$  is a constant along an isobar so  $\phi PV/NkT$  varies as  $\sim 1/T$ , and a log plot of  $\tau$  vs  $\phi PV/NkT$  represents an effective Arrhenius plot for the relaxation times (see Fig. 5(b)). The VFT and parabolic equations are fit to the data obtained from the fragile fluid densities, between the low and high pressure  $C_p$  maxima on the compression EOS. The Arrhenius equation is fit over the data from  $\phi$  at and above the high pressure  $C_p$  maximum. The VFT and Arrhenius equations fit the data over the fragile and strong regions respectively, and extending the data fitting region for either equation leads to a decrease in the quality of the fits, suggesting this system may well exhibit a fragile-strong dynamic crossover, similar to that observed in the 2D confined fluid. However, the parabolic law, which does not contain a fragile-strong crossover, describes the

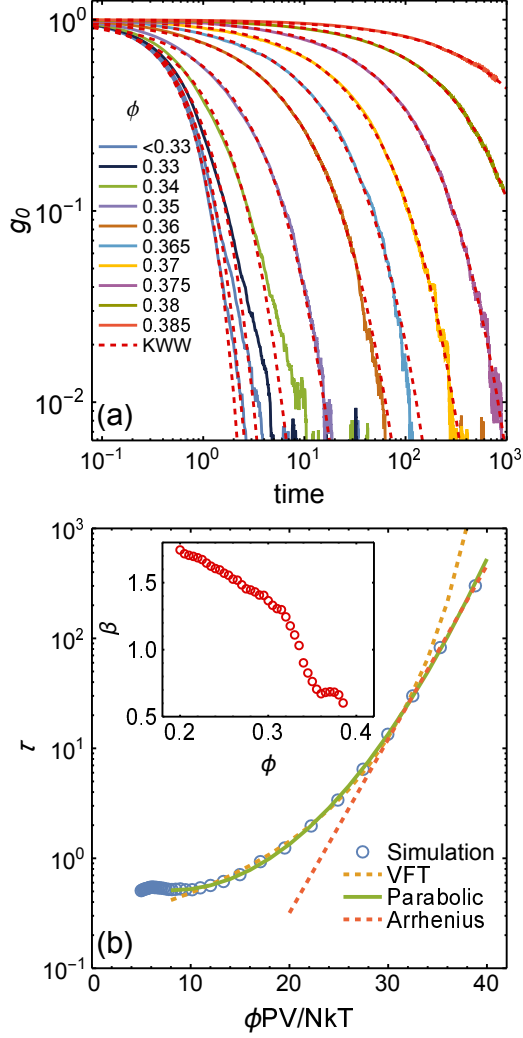


Figure 5: **Orientational structural relaxation in the compression branch.** (a) Log-Log plot of  $g_0$  for the compression branch as a function of time for different  $\phi$  from MD simulation (solid lines) and fits of the data to the KWW function (dashed lines). (b) Compression branch relaxation time,  $\tau$ , as a function of  $\phi PV/NkT$  with fits to the VFT, parabolic and Arrhenius equations. Inset: KWW exponent,  $\beta$ , obtained from fits to data in (a), as a function of  $\phi$ .

relaxation times over the entire range studied, despite only being fit using the data from below the  $C_p$  maximum.

A direct visualization of a trajectory, showing the structure and dynamics of the fluid, can be achieved by plotting the local twist direction of each particle as a function of time (Fig. 6). At low  $\phi$  ( $P_L/kT < 33$ ), the high defect fraction ensures that defects are generally closer than three particles, preventing the formation of the helix structure, and the fast particle dynamics means the tetrahedron associated with a particle frequently changes sign. With increasing density and pressure ( $P_L/kT = 70, 90$ ), along the compression branch of the EOS, the helical sections increase in length. We also see the diffusion of the defects, as well as the spontaneous creation and annihilation of defect pairs. However, at the highest pressure ( $P_L/kT = 120$ ) the defects are well separated and diffuse slowly, suggesting the system is in a glassy state.

### **Decompression branch: $\phi > 0.33$ , $P/kT > 38$**

The thermodynamics, structure and dynamics of the fluid along the decompression branch of the EOS are distinct from those of compressed fluid. The initial state of the system consists of a perfect helix with a  $\mathcal{P}$  twist direction, but as there is no bias in the system that would preferentially select one twist direction over the other, we obtain the same general results when decompressing from a perfect  $\mathcal{M}$  helix. As the system is decompressed, the heat capacity exhibits a broad feature at high pressures where  $\theta$  is essentially zero and  $f_{\mathcal{P}} \approx 1$  (See Fig. 2). At  $P_L/kT \approx 70$ ,  $\theta$  rapidly increases before plateauing as the decompression branch joins the compression branch when  $\theta \approx 0.25$ , leading to the sharp maximum in the  $C_p$  located at  $P_L/kT \approx 50$ . With increasing  $\theta$ , we also see  $f_{\mathcal{P}}$  decrease, but it remains non-zero. This implies the defects, which are generated in pairs, remain at least loosely paired so that the sections of  $\mathcal{M}$  helix created between the defects are small, allowing the  $\mathcal{P}$  tetrahedra to remain in excess until the equation of state finally reaches the compression branch and  $f_{\mathcal{P}}$  falls to zero.

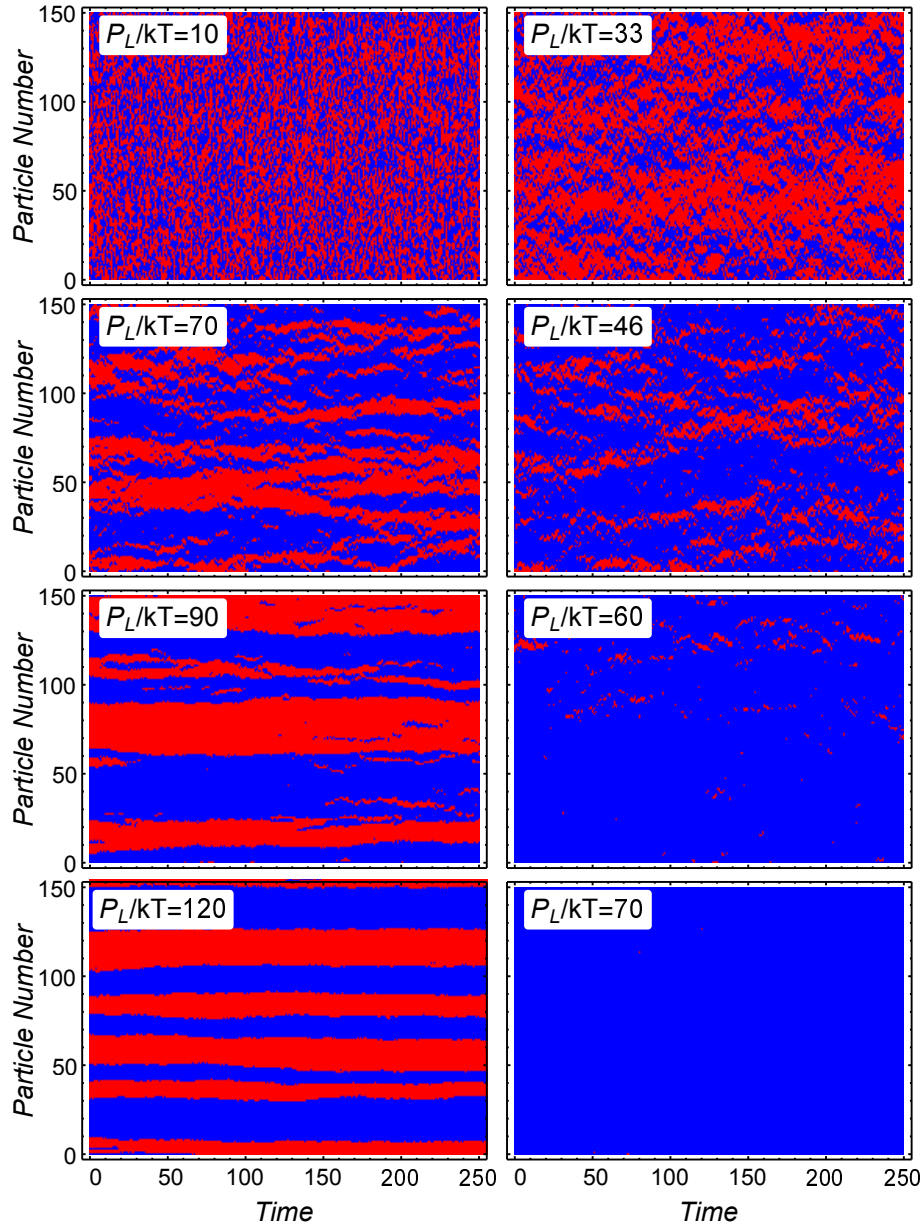


Figure 6: **Time evolution of fluid helical structure.** Structural evolution of a section of the fluid (particles 1-150) as a function of time with spheres described by a  $\mathcal{M}$  tetrahedron (red) and  $\mathcal{P}$  tetrahedron (blue), for the compression branch (Left Column) and the decompression branch (Right Column).

Figure 3(b) shows that  $P(n)$  in the decompression branch also exhibits important differences compared to that of the compression branch. At  $P_L/kT = 60$ , the distribution decays as a power law for small helical sections before eventually crossing over to an exponential decay for helical section sizes larger than  $n \approx 100$  (see insert Fig. 3(b)). With decreasing pressure, the crossover size moves to smaller  $n$  so the distribution begins to resemble that of the low pressure region of the compression branch where the entire distribution is exponential. It is not possible to measure the distribution at higher pressures as the defect fraction effectively goes to zero. While  $P(n)$  suggests there are non-trivial correlations in the helical structure of the system along the decompression branch, Figure 4(b) shows that the translational correlation decays exponentially, as expected. For pressures in the region,  $38 < P_L/kT < 70$ ,  $\xi$  is smaller in the decompression branch than in the compression branch, going through a minimum before it grows at higher pressure to become the largest translational correlation in the system. However, at these high densities, it is difficult to accurately measure the correlation lengths.

The trajectories for the decompression branch, pictured in Fig. 6, exhibit differences from those of the compression branch. At  $P_L/kT = 70$  there are essentially no defects. As the pressure decreases, defects appear in pairs that remain closely paired as they diffuse until they annihilate. The pairing of the defects ensures the excess of  $\mathcal{P}$  tetrahedra.

Finally, Fig. 7 shows that  $g_0$  no longer decays to zero, in contrast to the behaviour observed in the compression branch, but instead plateaus at a finite value of  $g_0$  that increases with increasing  $\phi$ . It is also interesting to note how quickly the difference in relaxation behaviour between the decompression and compression branches develops. At  $\phi = 0.33$  the two branches exhibit the same behaviour and have the same pressure. However, at  $\phi = 0.331$ , where the equations of state have only just separated, the decompression branch no longer decays to zero on the time scale of our simulation. Furthermore, the structural relaxation in the compression branch continues to decay to zero at even higher densities, despite being at a higher pressure where the fluctuations required for particle rearrangement should be more

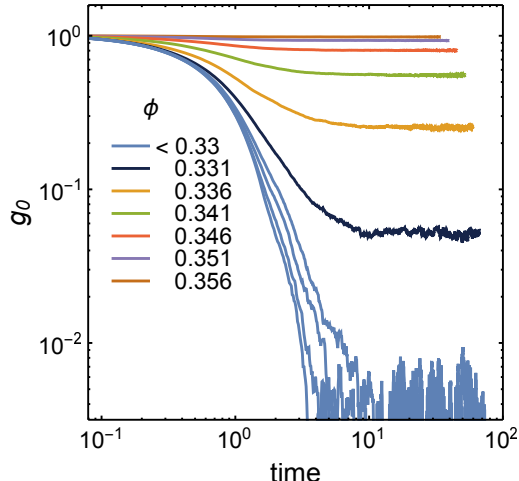


Figure 7: **Orientalional structural relaxation in the decompression branch.** Log-Log plot of  $g_0$  for the decompression branch as a function of time for different  $\phi$ .

difficult because of a reduced free volume.

## Discussion

Our results show the quasi-one-dimensional system of hard spheres confined to a narrow, cylindrical channel with diameter  $H_d/\sigma = 1.95$  has two branches to its EOS above  $P_L/kT \approx 38$ , ( $\phi \approx 0.33$ ) with distinct thermodynamic, structural and dynamic properties. It is not unusual for quasi-one-dimensional hard sphere systems to exhibit metastability and hysteresis<sup>14,17</sup> because at a given channel diameter the system may support structurally distinct ideal helical structures with different limiting densities. However, for channel diameters  $1 + \sqrt{3}/4/7 < H_d < 1 + 4\sqrt{3}/7$  there is only one perfect, single helical packing so the two branches of the EOS necessarily terminate at the same most dense packed structure.

Hu et al.<sup>46</sup> used the transfer matrix method to study the equation of state and correlation lengths of confined hard spheres with next nearest neighbour interactions up to  $P_L/kT \approx 50$ , and showed they did not exhibit a phase transition, consistent with the expectations for one and quasi-one-dimensional systems with short-ranged interactions. The analysis also found that the largest eigenvalue for the system, which determines the equilibrium



properties, consists of two conjugate eigenvalues at low pressure that split into two distinct real eigenvalues at an intermediate pressure. The correlation length associated with the largest eigenvalue continues to grow after the split, while the second largest correlation length goes through a minimum before growing again at higher pressure. The translational correlation lengths obtained in our simulations follow the same trend, allowing us to identify the compression branch of the EOS as the equilibrium state of the system. The pressure measured in our simulations along the compression branch is also the same as that predicted by the largest eigenvalue of the transfer matrix method. Furthermore,  $\xi$ , measured along the decompression branch follows the same evolution as the correlation length obtained for the smaller eigenvalue of the transfer matrix, which suggests the states are related, and implies the decompression branch represents a non-equilibrium or metastable state.

However, the EOS pictured in Fig. 1 then leads to a thermodynamic paradox. If there is no phase transition along either branch of the equation of state and both pressures vary continuously as a function of  $\phi$ , then the relative stability of the two states can be determined by comparing their Gibbs free energies,  $G/NkT = PV/NkT - S/Nk$ , at the same pressure. Figure 8 shows the difference in Gibbs free energies between the compression and decompression branches,  $\Delta G/NkT = G_c - G_d$ , where the entropy along each branch is calculated relative to the ideal gas at the same  $N, V$  and  $T$ ,

$$\Delta S(\phi)/Nk = \Delta S(\phi_r)/Nk - \int_{\phi_r}^{\phi} (PV/NkT - 1)d \ln \phi', \quad (1)$$

and the reference state occupied volume fraction,  $\phi_r < 0.33$ , is chosen to be below the bifurcation point in the EOS. The predicted free energy is positive, which would suggest the decompression branch is more stable, contradicting the transfer matrix results. One way to resolve the paradox would be to note that, as the system is compressed from below  $\phi \approx 0.33$ , it always follows the higher pressure branch. To make the system fall onto the lower pressure branch, it is necessary to impose a constraint that ensures defects are eliminated in a way

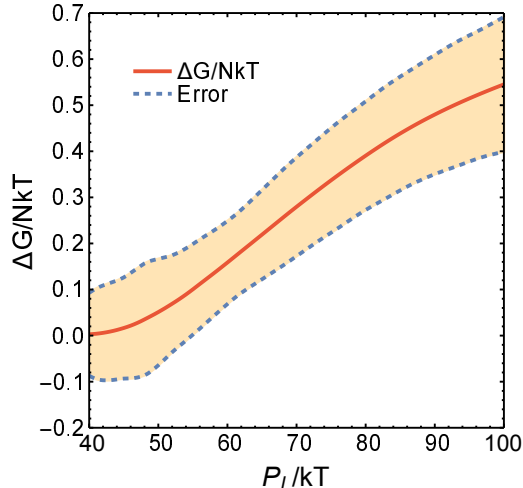


Figure 8: **Gibbs free energy.** The free energy difference between the compression and decompression branches,  $\Delta G/NkT$ , as a function of  $P_L/kT$  (solid line). Error estimates based on standard deviations in the EOS for both branches (dashed lines).

that leads to an excess in  $f_{\mathcal{P}}$ . This would reduce the entropy of the decompression branch making  $\Delta G/NkT < 0$ . If the entropy loss is large enough, then the decompression branch will be metastable over the entire pressure range, with  $\Delta G/NkT \rightarrow 0$ , from below only as  $P_L/kT \rightarrow \infty$  and the two branches approach the same most dense jammed packing. The low pressure/low density point where the two branches meet, then represents the low pressure limit of stability for the metastable state.

The way defects are organized within the fluid determines the topological properties of the system. It also has important consequences for the configurational and vibrational contributions to the entropy. An earlier study<sup>40</sup> of the jammed states of this system found that the packing density,  $\phi_J$ , of the system increases as two isolated defects approach each other. At a fixed  $\phi$  of the fluid, this leads to an increase in the vibrational entropy of the system that induces an effective long range attraction between the two defects. Along the compression branch, the defects in the fluid are arranged randomly, giving rise to the exponential decay of  $P(n)$ , and even at high densities, where the peaks in  $P(n)$  suggests there is at least some short-ranged attraction between defects, there is no preference for either helical twist direction, which ensures  $f_{\mathcal{P}}$  is always zero. This suggests the fluid is

stabilized by configurational entropy because the defects can be arranged in a large number of different ways.

On the other hand, the structure of the system along the decompression branch is intrinsically topological. The helical twist direction of the system is set by the initial condition. Defects in the helix appear in pairs that must remain loosely bound in order to preserve the excess twist. The defect pairs can appear though out the system, which helps retain a degree of configurational entropy, but there are still fewer available configurations than would be possible for a system with unpaired defects, at the same defect fraction. This suggests the decompression branch is stabilized through the increased vibrational entropy gained by keeping the defect close together. In fact, the degree of stabilization is such that the chiral excess phase persists down to low densities, where in principle the system has sufficient free volume to rearrange as demonstrated by the fast relaxation times of the higher pressure compression branch at the same  $\phi$ , and only terminates when there are enough defects ( $\theta = 0.25$ ) to effectively eliminate the helical sections altogether.

An attraction between topological defects is a key feature of the physics that leads to the KTHNY transition and hexatic phase in 2D hard discs,<sup>60-62</sup> which raises the question of whether or not the decompression branch of our quasi-1D system exhibits similar phenomena. Figure. 2(b) shows that  $\theta$  goes continuously to zero around  $P_L/kT \approx 70$ , which might suggest there is an ordering transition at high pressure along the decompression branch, even if it is metastable with respect the equilibrium branch. The helical correlations along the channel, captured by  $P(n)$ , also exhibit a power law decay over small  $n$ , where the crossover to exponential decay moves to larger  $n$  with increasing pressure. However, these may also simply reflect the difficulties associated with establishing the true metastable equilibrium along the decompression branch, particularly as the fraction of defects becomes small. In particular, the crossover to an exponential decay in  $P(n)$  confirms that the system remains fluid at the pressures studied. A similar crossover was recently observed in a quasi-one dimensional system of hard disks.<sup>63-65</sup> Studies with larger numbers of particles, along with

transfer matrix calculations performed at higher pressures, would be required to fully resolve the behaviour of the system at densities close to the most dense jammed state.

## Conclusion

Our results clearly show that the decompression branch remains metastable, with an excess twist direction, on the time scale of our simulation, despite being in a lower pressure state relative to the equilibrium branch. We also show that the topological properties of the fluid play an important role in maintaining its stability down to low densities where the two branches of the EOS meet, suggesting the decompression branch is in fact a topologically stabilized state. However, the fluid along the decompression branch is metastable and so will eventually decay over time. Simulation time scales are short in comparison to experimental time scales, so it remains to be seen if such a topologically stabilized state can be observed in real systems, and whether the phenomena can be found in other quasi-one-dimensional systems that have helical structure.

## Methods

### Model

We study a system of  $N$  hard spheres with diameter  $\sigma$ , confined in a cylindrical narrow channel of length  $L$  with channel diameter  $H_d/\sigma = 1.95$ , which ensures spheres can only contact their first and second neighbours in either direction along the channel. The particle–particle and particle–wall interaction potentials are given by,

$$U(r_{ij}) = \begin{cases} 0 & r_{ij} \geq \sigma \\ \infty & r_{ij} < \sigma \end{cases}, \quad (2)$$

$$U_w(r_i) = \begin{cases} 0 & |r_{xy}| \leq |H_0/2| \\ \infty & \text{otherwise} \end{cases}, \quad (3)$$

respectively, where  $r_{ij} = |\mathbf{r}_i - \mathbf{r}_j|$  is the distance between particles,  $|r_{xy}|$  is the magnitude of position vector for a particle perpendicular to the wall where the centre of the cylinder is located at  $x = y = 0$  and the longitudinal direction of the channel extends in the  $z$  direction. The volume accessible to the particles' centres is  $V_0 = \pi L(H_0/2)^2$ , where  $H_0 = H_d - \sigma$ , and the occupied volume is  $\phi = 2N\sigma^3 / (3LH_d^2)$ .

## Molecular Dynamics Simulation

Our study uses both molecular dynamics (MD) and Monte Carlo (MC) simulations with systems containing  $N = 10^4$  particles and  $H_d/\sigma = 1.95$ . The MD simulations are performed, in the canonical ensemble  $(N, V, T)$  using a modified version of the Lubachevsky and Stillinger event-driven algorithm<sup>66</sup> that compresses the system by expanding the particles and channel diameter such that  $H_d/\sigma$  remains constant. The unit of time for the simulation is given by  $\sigma\sqrt{m/kT}$ , where  $k_B$  is Boltzmann's constant and  $m$  is the mass of a particle, which is set to unity. Particles are assigned random velocities at the beginning of the run, scaled to ensure  $kT = 1$  and velocity rescaling is used to maintain the temperature. Depending on  $\phi$ ,  $200N - 10^6N$  collisions are used to reach equilibrium before data is collected over the next  $400N - 10^7N$  collisions.

Periodic boundary conditions for a helical system are described by,<sup>14</sup>

$$\mathbf{r}_{i\gamma} = \mathbf{r}_i + n_\gamma \boldsymbol{\lambda}, \quad (4)$$

where  $\mathbf{r}_{i\gamma}$  is the position of particle  $i$  in the  $\gamma^{\text{th}}$  unit cell,  $n_\gamma$  is an integer and  $\boldsymbol{\lambda}(\lambda_{|r_{xy}|}, \lambda_\alpha, \lambda_z)$  is the lattice vector for the radial, angular,  $\alpha$ , and longitudinal,  $z$ , components of the cylindrical coordinates, respectively. For the MD simulations, we use translational periodic boundaries with  $\lambda_z = L$  and  $\lambda_{|r_{xy}|} = \lambda_\alpha = 0$ , so there is no twist between cells.

At the start of each MD compression simulation, particles are placed in a linear lattice with  $\phi = 0.01$ . The system is equilibrated and data collected at each  $\phi$  before it is compressed to the next density at a compression rate of  $d\sigma/dt = 0.001$ . The MD decompression simulations begin at high density,  $\phi = 0.40$ , with the particles arranged in the perfect single helix packing containing a pair of defects so there are two helical sections containing  $N = 9998$  and  $N = 2$  particles, respectively. This is necessary because of the inherent twist associated with the perfect helical structure and the fact that we use translational periodic boundaries. The close packed, perfect helix has  $\phi = 0.421$ .

## Monte Carlo Simulation

Our MC simulations are carried out in the isobaric-isothermal ensemble where  $N$ ,  $T$  and  $P_L$ , the longitudinal pressure applied to the ends of the channel, are held fixed. We also employ helical periodic boundaries characterized by vector components  $\lambda_z = L$ ,  $\lambda_{|r_{xy}|} = 0$  and  $\lambda_\alpha = \alpha$ . Three types of MC move are used: particles are moved using the standard Metropolis algorithm, the volume is sampled in a logarithmic random walk<sup>67</sup> and we allow twist MC moves that uniformly sample the periodic boundary twist angle  $\alpha$ . The step size for each type of MC move is adjusted to ensure an acceptance rate of approximately 40%. In the simulations, a single MC cycle involves  $N$  particle moves,  $0.02N$  volume moves and  $0.02N$  twist moves. Our simulations are performed in blocks of  $5 \times 10^6$  MC cycles, so we can follow the system converging to equilibrium, and the results and errors are reported for the final block. The MC compression simulations compress the system at their final  $P_L$ , starting from a linear lattice with  $\phi = 0.01$ , so that each state point evolves independently from the others. The system is equilibrated for three MC blocks ( $1.5 \times 10^7$  MC cycles), before data is collected over the fourth MC block. The MC decompression simulations, performed at a fixed  $P_L$ , start from a perfect helix, with single right ( $\mathcal{P}$ ) twist direction, and the  $Z$ -coordinate scaled to the lower density. Here, the use of helical boundary conditions with a variable twist angle means there is no need to introduce a defect. The system is equilibrated

for 12 MC blocks and the results are reported for the 13th block. More details concerning the equilibration of the decompression branch are provided in the Supporting Information. We also note that our results for the decompression branch are not dependent on the choice of twist direction in the perfect helix.

## Heat Capacity

We calculate a number of thermodynamic and structural properties of the fluid. The constant pressure heat capacity for the system is given by,

$$\frac{C_p}{Nk} = \left( \frac{\partial H}{\partial T} \right)_{P_L} = \frac{3}{2} + \frac{Z}{1 + \left( \frac{\partial \ln Z}{\partial \ln \phi} \right)_T}, \quad (5)$$

where  $H$  is the enthalpy,  $Z = P_L AL/NkT$  is the compressibility factor and  $A$  is the cross sectional area of the cylinder.

## Helical Structure

To examine the helical structure of the fluid, we identify a local helical twist direction for each atom  $i$  based on the signed volume the tetrahedron given by;

$$v_{tet}(i) = \frac{\mathbf{a} \cdot \mathbf{b} \times \mathbf{c}}{6}, \quad (6)$$

where  $\mathbf{a}$ ,  $\mathbf{b}$  and  $\mathbf{c}$  are the position vectors for particles  $i - 1$ ,  $i$  and  $i + 1$ , relative to particle  $i + 2$ , respectively. Successive particles with the same sign for  $v_{tet}(i)$  have same helical twist direction, which allows us to identify the length of a helical section. Defects, located between helical sections with opposite twist directions, occur when  $v_{tet}$  changes sign. The method has been used to study helical structure in the jammed structures of this system,<sup>45</sup> where the method also uses the magnitude  $|v_{tet}|$ , which is distinguishably small for particles in the defect, to confirm the location of the defect. In the fluid, particles adopt configuration with

a broad distribution of  $|v_{tet}|$  so this is no longer possible. The current work identifies the location of the defects just using the sign changes of  $v_{tet}(i)$ .

Our analysis of the helical structure in the fluid represents an approximate mapping of a fluid configuration to a nearby jammed structure, effectively providing an inherent structure landscape<sup>42–44</sup> description for the system. However, we find cases where a pair of defects are located on neighbouring particles, which represents an unstable environment that leads to defect annihilation when compressed to jamming.<sup>40</sup> Both MD and MC simulations produce the same defect properties so in the results section we report the fraction of defects,  $\theta$  for the MC results including the neighbouring defects, and the MD results with the neighbouring defects eliminated.

We also calculate the probability,  $P(n)$ , of finding a helical section containing  $n$  particles and the excess fraction of  $\mathcal{P}$  tetrahedra,  $f_{\mathcal{P}}$ , as the difference in the number of right (positive  $v_{tet}$ ) tetrahedra and left (negative  $v_{tet}$ ) in a configuration normalized by  $N$ . Assuming the number and distribution of the defects in the fluid provide an effective instantaneous map of a configuration to its inherent structure, we can follow the evolution of the system through the inherent structure landscape (ISL) as a function of pressure and density.

## Structural Relaxation

Structural relaxation in the system occurs through the creation, diffusion and elimination of defects because these change the local direction of helical twist. To measure structural relaxation, we define a self correlation function,

$$g_0 = \left\langle \frac{v_{tet}(i, 0)}{|v_{tet}(i, 0)|} \frac{v_{tet}(i, t)}{|v_{tet}(i, t)|} \right\rangle, \quad (7)$$

where the average is taken over all particles and multiple time origins have been used.



## Acknowledgement

We would like to thank the Digital Alliance of Canada for computational resources. RKB acknowledges NSERC grant RGPIN–2019–03970 for financial support. This work was also supported by the Iran National Science Foundation (INSF) and the Iranian National Foundation of Elites via Grant No. 4015274.

## Supporting Information Available

Supporting information provides details regarding the convergence of the thermodynamic and structural properties of the system along the decompression branch.

## References

1. Senthil, T. Symmetry-Protected Topological Phases of Quantum Matter. *Annu. Rev. Conden. Matt. Phys.* **2014**, *6*, 1–26.
2. Kane, C. L.; Lubensky, T. C. Topological boundary modes in isostatic lattices. *Nat. Phys.* **2013**, *10*, 39–45.
3. Loehr, J.; Loenne, M.; Ernst, A.; Heras, D. d. l.; Fischer, T. M. Topological protection of multiparticle dissipative transport. *Nat. Commun.* **2016**, *7*, 11745.
4. Pedro, R. P.; Paulose, J.; Souslov, A.; Dresselhaus, M.; Vitelli, V. Topological Protection Can Arise from Thermal Fluctuations and Interactions. *Phys. Rev. Lett.* **2019**, *122*, 118001.
5. Zygmunt, W.; Teich, E. G.; Anders, G. v.; Glotzer, S. C. Topological order in densely packed anisotropic colloids. *Phys. Rev. E* **2019**, *100*, 032608.

6. Erickson, R. O. Tubular Packing of Spheres in Biological Fine Structure. *Science* **1973**, *181*, 705–716.
7. Harris, W. F.; Erickson, R. O. Tubular arrays of spheres: Geometry, continuous and discontinuous contraction, and the role of moving dislocations. *J. Theor. Biol.* **1980**, *83*, 215–246.
8. Pickett, G. T.; Gross, M.; Okuyama, H. Spontaneous Chirality in Simple Systems. *Phys. Rev. Lett.* **2000**, *85*, 3652–3655.
9. Mughal, A.; Chan, H. K.; Weaire, D. Phyllotactic Description of Hard Sphere Packing in Cylindrical Channels. *Phys. Rev. Lett.* **2011**, *106*, 115704.
10. Mughal, A.; Chan, H. K.; Weaire, D.; Hutzler, S. Dense packings of spheres in cylinders: Simulations. *Phys. Rev. E* **2012**, *85*, 051305.
11. Mughal, A.; Weaire, D. Theory of cylindrical dense packings of disks. *Phys. Rev. E* **2014**, *89*, 042307.
12. Fu, L.; Steinhardt, W.; Zhao, H.; Socolar, J. E. S.; Charbonneau, P. Hard sphere packings within cylinders. *Soft Matter* **2016**, *12*, 2505–2514.
13. Durán-Olivencia, F. J.; Gordillo, M. C. Ordering of hard spheres inside hard cylindrical pores. *Phys. Rev. E* **2009**, *79*, 061111.
14. Fu, L.; Bian, C.; Shields, C. W.; Cruz, D. F.; López, G. P.; Charbonneau, P. Assembly of hard spheres in a cylinder: a computational and experimental study. *Soft Matter* **2017**, *13*, 3296–3306.
15. Zhu, G.; Gao, L.; Xu, Z.; Dai, X.; Zhang, X.; Yan, L.-T. Entropy-Driven Unconventional Crystallization of Spherical Colloidal Nanocrystals Confined in Wide Cylinders. *Nano Lett.* **2021**, *21*, 8439–8446.

16. Winkelmann, J.; Haffner, B.; Weaire, D.; Mughal, A.; Hutzler, S. Simulation and observation of line-slip structures in columnar structures of soft spheres. *Phys. Rev. E* **2017**, *96*, 012610.
17. Mughal, A.; Winkelmann, J.; Weaire, D.; Hutzler, S. Columnar structures of soft spheres: Metastability and hysteresis. *Phys. Rev. E* **2018**, *98*, 043303.
18. Mickelson, W.; Aloni, S.; Han, W.-Q.; Cumings, J.; Zettl, A. Packing C60 in Boron Nitride Nanotubes. *Science* **2003**, *300*, 467–469.
19. Khlobystov, A. N.; Britz, D. A.; Ardavan, A.; Briggs, G. A. D. Observation of Ordered Phases of Fullerenes in Carbon Nanotubes. *Phys. Rev. Lett.* **2004**, *92*, 245507.
20. Yao, Z.; Liu, C.-J.; Lv, H.; Liu, B.-B. Stable double helical iodine chains inside single-walled carbon nanotubes. *Phys. Lett. A* **2016**, *380*, 2781–2785.
21. Lohr, M. A.; Alsayed, A. M.; Chen, B. G.; Zhang, Z.; Kamien, R. D.; Yodh, A. G. Helical packings and phase transformations of soft spheres in cylinders. *Phys. Rev. E* **2010**, *81*, 040401.
22. Jiang, L.; de Folter, J. W. J.; Huang, J.; Philipse, A. P.; Kegel, W. K.; Petukhov, A. V. Helical Colloidal Sphere Structures through Thermo-Reversible Co-Assembly with Molecular Microtubes . *Angewandte Chemie Int. Ed.* **2013**, *52*, 3364–3368.
23. Jiménez-Millán, S.; García-Alcántara, C.; Ramírez-Hernández, A.; Sambriski, E.; Hernández, S. Self-Assembly of core-corona colloids under cylindrical confinement: A Monte Carlo study. *J. Mol. Liq.* **2021**, *335*, 116219.
24. Meagher, A.; García-Moreno, F.; Banhart, J.; Mughal, A.; Hutzler, S. An experimental study of columnar crystals using monodisperse microbubbles. *Colloids Surf A: Physicochem. Eng. Asp.* **2015**, *473*, 55–59.

25. Jin, W.; Chan, H.-K.; Zhong, Z. Shape-Anisotropy-Induced Ordered Packings in Cylindrical Confinement. *Phys. Rev. Lett.* **2020**, *124*, 248002.
26. Wan, S.; Xi, X.; Zhang, H.; Ning, J.; Zheng, Z.; Zhang, Z.; Long, Y.; Deng, Y.; Fan, P.; Yang, D.; Li, T.; Dong, A. Shape-Mediated Oriented Assembly of Concave Nanoparticles under Cylindrical Confinement. *ACS Nano* **2022**, *16*, 21315–21323.
27. Vlasov, Y. A.; Bo, X.-Z.; Sturm, J. C.; Norris, D. J. On-chip natural assembly of silicon photonic bandgap crystals. *Nature* **2001**, *414*, 289–293.
28. Zhao, Y.; Shang, L.; Cheng, Y.; Gu, Z. Spherical Colloidal Photonic Crystals. *Accounts Chem. Res.* **2014**, *47*, 3632–3642.
29. Lei, Q.-l.; Ni, R.; Ma, Y.-q. Self-Assembled Chiral Photonic Crystals from a Colloidal Helix Racemate. *ACS Nano* **2018**, *12*, 6860–6870.
30. Wan, D.; Glotzer, S. C. Randomness in self-assembled colloidal crystals can widen photonic band gaps through particle shape and internal structure. *arXiv* **2020**,
31. Liu, T.; Chan, H.-K.; Wan, D. Chiral photonic crystals from sphere packing. *arXiv* **2023**,
32. Hove, L. v. Sur L'intégrale de Configuration Pour Les Systèmes De Particules À Une Dimension. *Physica* **1950**, *16*, 137–143.
33. Ruelle, D. Statistical mechanics of a one-dimensional lattice gas. *Commun.math. Phys.* **1968**, *9*, 267–278.
34. Landau, L.; Lifshitz, E. *Statistical Physics, Part 1. Course of Theoretical Physics Volume 5* ; Oxford ; New York : Pergamon Press; 1980.
35. Cuesta, J. A.; Sánchez, A. General Non-Existence Theorem for Phase Transitions in One-Dimensional Systems with Short Range Interactions, and Physical Examples of Such Transitions. *J. Stat. Phys.* **2004**, *115*, 869–893.

36. Saryal, S.; Klamsner, J. U.; Sadhu, T.; Dhar, D. Multiple Singularities of the Equilibrium Free Energy in a One-Dimensional Model of Soft Rods. *Phys. Rev. Lett.* **2018**, *121*, 240601.
37. Dyson, F. J. Existence of a phase-transition in a one-dimensional Ising ferromagnet. *Commun.math. Phys.* **1969**, *12*, 91–107.
38. Thouless, D. J. Long-Range Order in One-Dimensional Ising Systems. *Phys. Rev.* **1969**, *187*, 732–733.
39. Kosterlitz, J. M. Nobel Lecture: Topological defects and phase transitions. *Rev. Mod. Phys.* **2017**, *89*.
40. Yamchi, M. Z.; Bowles, R. K. Helical Defect Packings in a Quasi-One-Dimensional System of Cylindrically Confined Hard Spheres. *Phys. Rev. Lett.* **2015**, *115*, 025702.
41. Chan, H.-K.; Wang, Y.; Han, H. Densest helical structures of hard spheres in narrow confinement: An analytic derivation. *AIP Advances* **2019**, *9*, 125118.
42. Stillinger, F. H.; DiMarzio, E. A.; Kornegay, R. L. Systematic Approach to Explanation of the Rigid Disk Phase Transition. *J. Chem. Phys.* **1964**, *40*, 1564–1576.
43. Stillinger, F. H.; Weber, T. A. Hidden structure in liquids. *Phys. Rev. A* **1982**, *25*, 978–989.
44. Ashwin, S. S.; Yamchi, M. Z.; Bowles, R. K. Inherent Structure Landscape Connection between Liquids, Granular Materials, and the Jamming Phase Diagram. *Phys. Rev. Lett.* **2013**, *110*, 145701.
45. Zarif, M.; Spiteri, R. J.; Bowles, R. K. Inherent structure landscape of hard spheres confined to narrow cylindrical channels. *Phys. Rev. E* **2021**, *104*, 064602.
46. Hu, Y.; Fu, L.; Charbonneau, P. Correlation lengths in quasi-one-dimensional systems via transfer matrices. *Mol. Phys.* **2018**, *116*, 3345–3354.

47. Tari,; Ahmet, *The specific heat of matter at low temperatures*; World Scientific, 2003.
48. Kohlrausch,; R., Theorie des elektrischen Rückstandes in der Leidener Flasche. *Annalen der Physik* **1854**, *167*, 179–214.
49. Williams, G.; Watts, D. C. Non-symmetrical dielectric relaxation behaviour arising from a simple empirical decay function. *Trans. Faraday Soc.* **1970**, *66*, 80–85.
50. Debenedetti, P. G.; Stillinger, F. H. Supercooled liquids and the glass transition. *Nature* **2001**, *410*, 259.
51. Wu, J. H.; Jia, Q. The heterogeneous energy landscape expression of KWW relaxation. *Scientific Reports* **2016**, *6*, 20506.
52. Bouchaud, J.-P. In *Anomalous Relaxation in Complex Systems: From Stretched to Compressed Exponentials, in Anomalous Transport Foundations and Applications*; Klages,, Radons, G., Sookolov, M., Eds.; Wiley-VCH Verlag GmbH & Co.: KGaA, Weinheim.
53. Angell, C. A. Formation of Glasses from Liquids and Biopolymers. *Science* **1995**, *267*, 1924–1935.
54. Vogel, D. H. Das Temperaturabhaengigkeitsgesetz der Viskositaet von Fluessigkeiten. *Phys. Zeit.* **1921**, *22*, 645.
55. Fulcher, G. Analysis of Recent Measurements of the Viscosity of Glasses. *J. Am. Chem. Soc.* **1925**, *8*.
56. Tammann, G.; Hesse, W. Die Abhängigkeit der Viscosität von der Temperatur bei unterkühlten Flüssigkeiten. *Z. Anorg. Allge. Chem.* **1926**, *156*, 245–257.
57. Elmatad, Y. S.; Chandler, D.; Garrahan, J. P. Corresponding States of Structural Glass Formers. *J. Phys. Chem. B* **2009**, *113*, 5563–5567.

58. Elmatad, Y. S.; Chandler, D.; Garrahan, J. P. Corresponding States of Structural Glass Formers. II. *J. Phys. Chem. B* **2010**, *114*, 17113–17119.
59. Yamchi, M. Z.; Ashwin, S. S.; Bowles, R. K. Fragile-Strong Fluid Crossover and Universal Relaxation Times in a Confined Hard-Disk Fluid. *Phys. Rev. Lett.* **2012**, *109*, 225701.
60. Bernard, E. P.; Krauth, W. Two-Step Melting in Two Dimensions: First-Order Liquid-Hexatic Transition. *Phys. Rev. Lett.* **2011**, *107*, 155704.
61. Kapfer, S. C.; Krauth, W. Two-Dimensional Melting: From Liquid-Hexatic Coexistence to Continuous Transitions. *Phys. Rev. Lett.* **2014**, *114*, 035702.
62. Thorneywork, A. L.; Abbott, J. L.; Aarts, D. G. A. L.; Dullens, R. P. A. Two-Dimensional Melting of Colloidal Hard Spheres. *Phys. Rev. Lett.* **2017**, *118*, 158001.
63. Huerta, A.; Bryk, T.; Pergamenschik, V. M.; Trokhymchuk, A. Kosterlitz-Thouless-type caging-uncaging transition in a quasi-one-dimensional hard disk system. *Phys. Rev. Res.* **2020**, *2*, 033351.
64. Hu, Y.; Charbonneau, P. Comment on “Kosterlitz-Thouless-type caging-uncaging transition in a quasi-one-dimensional hard disk system”. *Phys. Rev. Res.* **2021**, *3*, 038001.
65. Trokhymchuk, A.; Pergamenschik, V. M.; Huerta, A.; Bryk, T. Reply to “Comment on ‘Kosterlitz-Thouless-type caging-uncaging transition in a quasi-one-dimensional hard disk system’ ”. *Phys. Rev. Res.* **2021**, *3*, 038002.
66. Lubachevsky, B. D.; Stillinger, F. H. Geometric properties of random disk packings. *J. Stat. Phys.* **1990**, *60*, 561–583.
67. Frenkel, D.; Smit, B. Understanding Molecular Simulation: From Algorithms to Applications. *Academic Press, New York* **2002**,

# Supplemental Material: Convergence of Decompression Branch

Structural relaxation occurs rapidly along the high pressure equilibrium compression branch of the EOS (see Fig 5 of main text) and the measurements of the fluid properties converge quickly. However, structural relaxation along the decompression is slow so to follow the convergence of a thermodynamic or structural property we calculate its percentage change between MC cycles,

$$\% \Delta X = 100 \left( 1 - \frac{X(i-1)}{X(i)} \right). \quad (\text{S1})$$

Figures S1 and S1 show the evolution of  $\phi$  and  $\theta$ , respectively, as a function of MC cycle, starting from the perfect expanded helix. The largest changes in both quantities occur at pressures near the bifurcation of the two branches in the EOS ( $P_L/kT \approx 40$ ) as the system moves to lower density as it develops more defects. At high pressure, we actually see  $\phi$  increase. Above  $P_L/kT \approx 70$ , the system does not develop defects and the density increase is the result of a simple compression of the perfect helix. However, at pressures just below this we see the system develop defects while still increasing its density. This is somewhat surprising as the equilibrium branch is located at lower density. The density of the system appears to have converged, and is fluctuating around its equilibrium value, by time we reached the conclusion of our simulation, but we notice the number of defects continues to increase slowly, above the bifurcation point, although at a very slow rate.



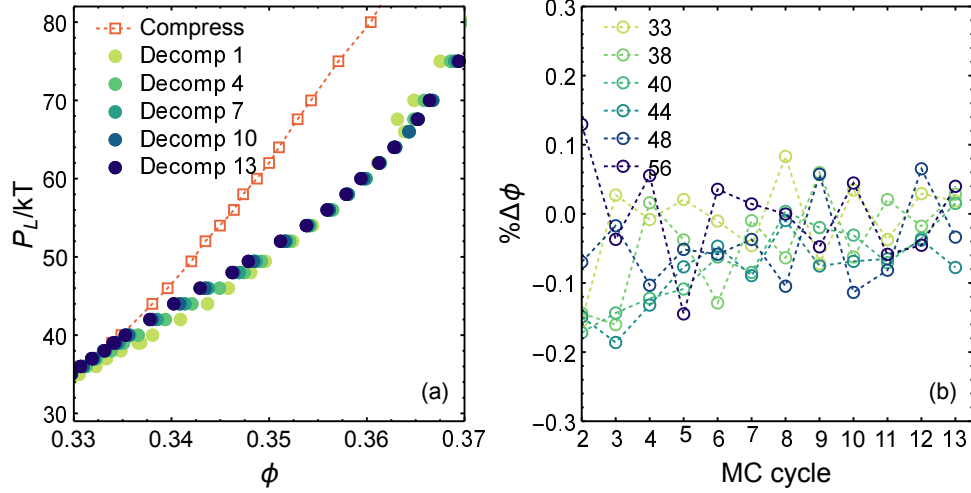


Figure S1: (a) Pressure,  $P_L/kT$  as a function of  $\phi$  at various MC cycles, along the decompression branch (circles), compares to the equilibrium compression branch pressure (squares). (b)  $\% \Delta \phi$  (See Eq. S1) as a function of MC cycle.

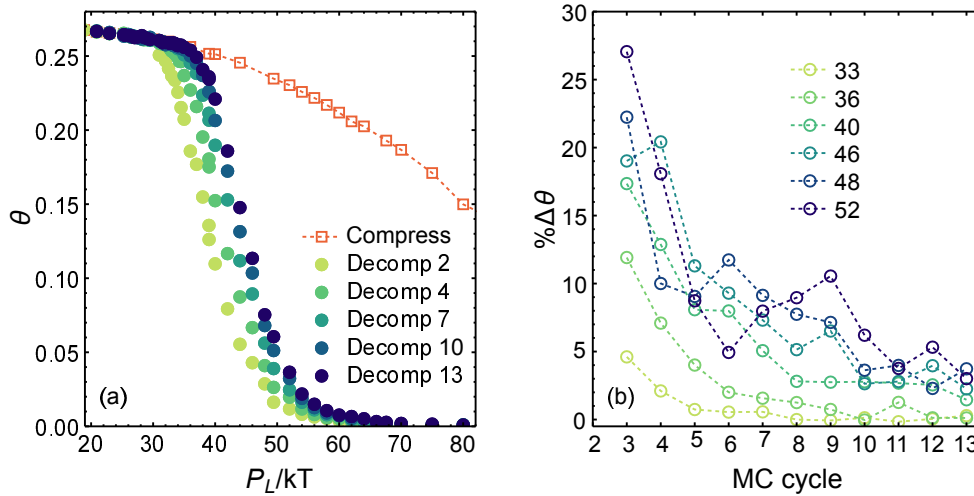


Figure S2: (a) Defect fraction  $\theta$  as a function of  $P_L/kT$  at various MC cycles, along the decompression branch (circles), compares to the equilibrium compression branch pressure (squares). (b)  $\% \Delta \theta$  (See Eq. S1) as a function of MC cycle.